Nanoscale Advances

ROYAL SOCIETY OF CHEMISTRY

PAPER

View Article Online
View Journal

Cite this: DOI: 10.1039/d6na00063k

Reduced hot-electron energy-loss rate induced by finite-square confinement potential in GaN/AlN, GaAs/AlAs, and GaSb/InAs nanostructured materials

Ho Kim Dan, [ab] Pham Tuan Vinh,[c] Le Phuong Long, [d] Huynh Thi Phuong Thuy[e] and Nguyen Dinh Hien *[fg]

This study offers a thorough and systematic examination of the hot electron energy-loss rate (ELR) within GaSb/InAs, GaAs/AlAs, and GaN/AlN finite-square geometrical QWs owing to electron–longitudinal optical (LO)–phonon coupling *via* the Fröhlich interaction under a quantizing magnetic field by using the electron-temperature-based formalism. Synchronously, the findings obtained in these GaSb/InAs, GaAs/AlAs, and GaN/AlN finite-depth-well confinement layers are compared to infinite-depth-well counterparts. The primary outcomes are derived as the following: the analytical formulation governing the ELR in GaSb/InAs, GaAs/AlAs, and GaN/AlN finite-depth QWs is derived by explicitly calculating for the optic-phonon interaction of hot-electrons. The results derived from the numerical study clarify how the hot-electron ELR responds to variation not only in the Landau-quantizing field, the well-layer thickness, and the effective-carrier temperature but also the surface-carrier density. Our evidence findings establish that among the GaSb/InAs, GaAs/AlAs, and GaN/AlN finite-depth QW materials considered, the GaN/AlN-based QW delivers the strongest hot-electron ELR response, the GaAs/AlAs-based counterpart follows with a reduced magnitude, while the GaSb/InAs-based QW yields the weakest dissipation. Concurrently, the derived results confirm that a finite-square confining potential markedly suppresses the hot-electron ELR in GaSb/InAs, GaAs/AlAs, and GaN/AlN QWs when compared with their infinite-depth counterparts. The ELR within QW heterostructures is appreciably impacted by confinement potentials. This highlights the important role of quantum confinement engineering in controlling 2D electronic energy relaxation. Therefore, adjusting the confinement potential shape or the quantum well depth can effectively enhance hot-electron dynamics and overall device efficiency within QW-based optoelectronic applications, without changing the materials. This work opens up promising avenues for advancing optoelectronic devices employing finite-square confining potential QWs.

Received 24th January 2026
Accepted 24th May 2026

DOI: 10.1039/d6na00063k

rsc.li/nanoscale-advances

1. Introduction

The energy-loss rate of hot-electrons in low-dimensional structured semiconductors provides a direct measure of electron–phonon interactions and carrier thermalization processes. Quantifying ELR in such heterostructures of hot electrons enables the identification of dominant scattering mechanisms and reveals how quantum confinement influences electron cooling dynamics. In many practical device configurations, the applied electric fields are sufficiently strong to drive carriers into highly non-equilibrium states, resulting in electron temperatures that substantially exceed that of the host lattice. Under such conditions, the effective thermal state of the carriers is dictated primarily by their phonon emission dynamics. Consequently, a detailed understanding of the underlying electron–phonon (e–ph) coupling mechanisms becomes essential for describing energy relaxation and transport behavior in these systems. Recent advancements in fabrication techniques have propelled low dimensional nanostructures into the spotlight within semiconductor physics. In which, electronic features are influenced by unlike scattering mechanisms. Notably, the e–p scattering mechanism evidently influences the hot-electron ELR as well as transport-features within polar-nanostructures.[1–3] In very recent studies, we employed an electronic temperature approach to evaluate

[a]Optical Materials Research Group, Science and Technology Advanced Institute, Van Lang University, Ho Chi Minh City, Vietnam. E-mail: hokimdan@vlu.edu.vn
[b]Faculty of Applied Technology, School of Technology, Van Lang University, Ho Chi Minh City, Vietnam
[c]Division of Physics, School of Education, Dong Thap University, Cao Lanh 870000, Vietnam
[d]Center of Scientific Research and Application, Lac Hong University, No.10 Huynh Van Nghe Str., Tran Bien Ward, Dong Nai Province, Vietnam
[e]Thu Dau Mot University, Binh Duong Province, Vietnam
[f]Institute of Research and Development, Duy Tan University, Da Nang, Vietnam
[g]School of Engineering & Technology, Duy Tan University, Da Nang, Vietnam. E-mail: nguyendinhhien2@duytan.edu.vn

ELR is induced by optic phonon scattering, distinguishing contributions from bulk-and confined-phonons in GaAs and III-nitride infinite square QWs.[4,5] A comparative analysis of zinc- and cadmium-based quasi-two-dimensional materials further demonstrated that well-thickness, two-dimensional electronic density, electron-temperature, and quantizing magnetic fields critically affect ELR, offering guidance for material selection and device optimization.[5,6] Controlling ELR is central for optoelectronic device design. Slow energy dissipation can extend hot-carrier lifetimes in solar cells or photodetectors, whereas accelerated cooling reduces noise in high frequency operation.[4,5] High-field measurements provide insight into non equilibrium dynamics, enabling precise modelling of electron relaxation under extreme conditions. Additional theoretical and experimental investigations expand the understanding of ELR across diverse nanostructures within diverse confinement potentials. Makhfudz *et al.*[7] showed that quantum confinement reduces the thermalization power required to maintain quasi-equilibrium hot carriers in solar cells, while coherent phonon modes in superlattices suppress e–ph scattering, prolonging hot carrier lifetimes.[8] Besides, in graphene, inelastic scattering with acoustic, optical, and surface polar optic phonons can significantly affect the hot-electron ELR.[9] Broadband cooling spectra of PbSe quantum dots further reveal energy-dependent relaxation dynamics for both electrons and holes, illustrating the impact of discrete electronic states on carrier thermalization.[10] In brief, these findings indicate that systematic ELR characterization provides fundamental insight into scattering processes and informs the engineering of low-dimensional materials with tunable hot-carrier dynamics, critical for high-efficiency nanoscale devices. Consequently, there is a strong impetus to pursue expanded, comparative, and methodical studies of energy-relaxation dynamics of hot carriers in nanostructured semiconductor platforms, as such insights directly support the refinement of high-performance electronic and optoelectronic technologies. Researches of hot-electron energy dissipation in QW heterostructures have shown that relaxation strength is strongly influenced by the well geometry and the vibrational spectrum supported by the material system. In early measurements on a single GaAs/$Al_xGa_{1-x}As$ QW, the threshold for LO-phonon emission was shown to mark a major drop in electronic temperature, as electrons above that energy couple rapidly to the optic-phonon channel.[11,12] Subsequent analyses of GaInNAs/GaAs modulation-doped QWs pointed out that whether phonon modes are bulk, interface, or confined influences total cooling efficiency and alters the balance of scattering pathways.[13,14] More recent experimental studies in alloy-based Q-2D heterostructures of ZnS/ZnSe/ZnTe or CdS/CdSe/CdTe revealed that composition, barrier height, and interface quality can markedly tune the hot-electron loss rate and thereby permit engineered control of relaxation in the heterostructure.[4,6] Furthermore, loss-rate measurements under strong magnetic quantization in similarly confined QW systems disclosed oscillatory patterns tied to transitions between discrete Landau levels, indicating that magnetic confinement reshapes the available phonon and electron coupling channels.[5] Comparative investigations across II–VI and III–V material families demonstrated a trend: systems with softer longitudinal optical phonons typically exhibit lower dissipation power, whereas those with rigid vibrational lattices support tighter coupling to the lattice and hence faster energy loss.[5] Collectively, these outcomes confirm that quantum wells offer a versatile platform for tailoring hot-electron cooling by deliberate design of both structural and phononic degrees of freedom. Although substantial progress has been made in analyzing hot-electron energy dissipation in III–V and II–VI QW heterostructures, most prior work has concentrated on systems with moderate band offsets, relatively simple vibrational spectra, or weak internal electric fields. As a result, the hot-electron energy-loss rate in finite square QWs formed from wide-band-gap nitrides such as GaN/AlN, or from polar and narrow-gap combinations such as GaAs/AlAs and GaSb/InAs, remains insufficiently explored. These material systems possess substantially stronger built-in electric fields, sharper band discontinuities, and distinct electron–phonon coupling characteristics compared with the more conventional wells that dominate the literature, suggesting that their relaxation behavior may deviate significantly from those systems. However, systematic studies of hot-electron cooling of finite square QWs based on these material platforms remain open. This gap underscores the need for detailed research of energy dissipation in GaN/AlN, GaAs/AlAs, and GaSb/InAs wells, particularly under conditions where strong built-in fields and pronounced band offsets act concurrently. Finite square QWs themselves are integral to a wide range of quantum engineered technologies. Their sharply defined potential profiles and adjustable barrier parameters permit precise manipulation of sub-band energies, optical transition strengths, and transport characteristics. Consequently, such wells are widely used in high-speed electronic devices, resonant-tunnelling structures, quantum-cascade designs, and terahertz emitters, as well as in quantum technology in the near future. Because the hot-electron energy-loss rate directly influences switching speed, gain bandwidth, thermal stability, and spectral response, accurate characterization of ELR in finite-depth wells is essential for predictive device modeling. Beyond the importance of the confining geometry, the specific material systems GaN/AlN, GaAs/AlAs, and GaSb/InAs each play a central role in key device technologies. GaN/AlN wells support high-electron-mobility transistors applied in power and RF electronics, benefiting from wide bandgaps, high breakdown fields, and elevated electron velocities.[15,16] Moreover, GaN-based heterostructures continue to attract significant attention due to their suitability for advanced applications encompassing high-power electronic devices, modern optoelectronic components, and emerging spintronic architectures. Enhancing the intrinsic material quality of GaN and establishing a deeper microscopic understanding of its charge-transport behavior remain essential steps toward realizing devices with superior operational efficiency and long-term performance stability.[17] In addition, wide-band-gap nitride platforms, such as GaN and its alloy families, serve as foundational materials for numerous advanced device concepts, including power-efficient electronic systems, compact light emitting structures, and robust photonic sources. Their technological value is accompanied by complex underlying physics, as the interplay of confinement effects, strain-driven lattice distortions, and anisotropic bonding environments strongly influences their electronic response. A thorough understanding of these factors is therefore essential for the development

of nano-scale components capable of sustaining high stability and superior operational characteristics. GaAs/AlAs QWs underpin resonant-tunneling diodes, quantum-cascade lasers, and terahertz oscillators, exploiting quantized states and sharp band offsets for ultrafast transport and frequency generation.[18,19] GaSb/InAs wells, known for their favorable band alignment and high electron mobility, are widely used in mid- and long-wavelength infrared photodetectors and form the basis of tunnel field-effect transistors and high-mobility devices for low-voltage operation. Recent work by Knox *et al.* demonstrated that scattering processes in InAs/GaSb coupled wells are highly sensitive to interface disorder and carrier density, underscoring the importance of accurately characterizing energy-loss mechanisms when designing infrared and high-speed device platforms.[20] These applications collectively highlight the technological significance of establishing a comprehensive understanding of hot-electron energy-loss processes in finite rectangular wells constructed from GaN/AlN, GaAs/AlAs, and GaSb/InAs. The present investigation undertakes a comprehensive and methodically organized examination of the hot-electron energy loss behavior within the GaSb/InAs, GaAs/AlAs, and GaN/AlN quantum structures exhibiting finite-square confinement geometry. Emphasis is placed on quantifying the dissipation characteristics shaped by optic-phonon coupling when carriers are subjected to a strong sufficient magnetic field to induce Landau level, employing an electron-temperature-based formulation to capture the nonequilibrium response. In parallel, the outcomes identified in these finite-depth-well heterolayer configurations are contrasted with those associated with their corresponding idealized, infinite-barrier realizations as reported in ref. 4 and 5 to elucidate confinement-induced modifications in the relaxation dynamics. In this work, the electron-temperature-based formalism provides a physically transparent and computationally efficient description of steady-state nonequilibrium carrier relaxation. Where the electron distribution is characterized by an effective temperature T_e, justified by the rapid electron–electron thermalization. While more advanced methods, such as Monte Carlo or Boltzmann transport approaches, offer a more detailed treatment, they involve significantly higher computational effort. The electron temperature model allows for the direct incorporation of electron confinement effects while retaining the dominant Fröhlich interaction with bulk LO-phonons, which is essential for identifying confinement potential-induced modifications of the electron-temperature-based formalism in finite *versus* infinite square quantum wells. The sections of this research are arranged in the following manner: the core theoretical description for the GaSb/InAs, GaAs/AlAs, and GaN/AlN finite-square geometrical QWs employed in our research is set out in Section 2. A description of the electron-temperature-based formalism is in Section 3. Following, Section 4 details the primary analytical findings concern the ELR in GaSb/InAs, GaAs/AlAs, and GaN/AlN finite-depth-well confinement heterolayers of hot electrons owing to optic-phonon interaction under the formalism based on carrier temperature. Finally, results derived from the numerical study and the corresponding discussion, including the obtained findings comparison in GaSb/InAs, GaAs/AlAs, and GaN/AlN finite-depth-well confinement heterolayers with those in infinite-depth-well counterparts, are summarized in Section 5.

2. The electron-temperature-based formalism

The electron-temperature framework is employed to evaluate the carrier energy-loss rate in this work. Within this approach, the electronic states follow a Fermi–Dirac distribution characterized by the $\mathcal{T}_e$-effective-carrier temperature, which exceeds the $\mathcal{T}_\ell$-lattice-temperature. This assumption allows the ELR to be computed within a closed formalism, where the deviation between $\mathcal{T}_e$ and $\mathcal{T}_\ell$ quantifies the degree of electronic heating. Under these non-equilibrium conditions, the mean power dissipated by the electrons, denoted ELR, can be expressed as[21–23]

$$\mathrm{ELR} = \left\langle \frac{\mathrm{d}\mathcal{E}}{\mathrm{d}t} \right\rangle = \frac{1}{N_e^S} \sum_{\mathbf{q}} \hbar\omega_{\mathbf{q}} \left(\frac{\partial \mathcal{F}_{\mathbf{q}}}{\partial t} \right)_{\mathrm{el-op}}, \tag{1}$$

with N_e^S is the surface-carrier density, $\hbar\omega_{\mathbf{q}}$ and $\mathbf{q} = (\mathbf{q}_\perp, q_z)$ the OP energy and wave-vector. $\mathcal{F}_{\mathbf{q}}$ representing the corresponding non-equilibrium distribution function of the OP. In the case where, the change rate of $\mathcal{F}_{\mathbf{q}}$ owing to op–el interaction, *i.e.*, the factor $(\partial \mathcal{F}_{\mathbf{q}}/\partial t)_{\text{el-op}}$ in eqn (1), is given in the following formalism:[5,23]

$$\frac{\partial \mathcal{F}_{\mathbf{q}}}{\partial t} = \sum_{\mathrm{i,f}} \{ \mathcal{P}_{\mathrm{em}} \mathcal{F}(\mathcal{E}_{\mathrm{f}}, \mathcal{T}_e)[1 - \mathcal{F}(\mathcal{E}_{\mathrm{i}}, \mathcal{T}_e)] - \mathcal{P}_{\mathrm{ab}} \mathcal{F}(\mathcal{E}_{\mathrm{i}}, \mathcal{T}_e)[1 - \mathcal{F}(\mathcal{E}_{\mathrm{f}}, \mathcal{T}_e)] \}, \tag{2}$$

in this formulation, the carrier's scattering rate associated with emitting/absorbing optic-phonon is $\mathcal{P}_{\mathrm{em}}/\mathcal{P}_{\mathrm{ab}}$. The electronic occupation in the initial (i) or final (f) state is specified by the Fermi-Dirac factor $\mathcal{F}(\mathcal{E}_{\mathrm{i/f}}, \mathcal{T}_e)$, where the $\mathcal{T}_e$ effective-carrier temperature characterizes the nonequilibrium carrier ensemble. With these definitions, the single-particle scattering probability per unit time can be evaluated applying the golden-rule of Fermi, which yield

$$\mathcal{P}_{\mathrm{em/ab}}(\mathrm{i} \to \mathrm{f}) = \frac{2\pi \left| \langle \mathrm{f} | H_{\mathrm{el-op}} | \mathrm{i} \rangle \right|^2 \delta(\mathcal{E}_{\mathrm{f}} - \mathcal{E}_{\mathrm{i}} \mp \hbar\omega_{\mathbf{q}})}{\hbar}. \tag{3}$$

In this framework, the coupling between charge carriers and optic-phonons is introduced through the interaction operator $H_{\mathrm{el-op}}$, which specifies the part of the total Hamiltonian responsible for the el–op scattering process in GaSb/InAs, GaAs/AlAs, and GaN/AlN finite-square geometrical QWs, and it appears as:[24]

$$H_{\mathrm{el-op}} = \sum_{\mathbf{q}} \left[\Upsilon_{\mathbf{q}} \vartheta_{\mathbf{q}} \, \mathrm{e}^{i\mathbf{q}\times\mathbf{r}} + \Upsilon_{\mathbf{q}}^* \vartheta_{\mathbf{q}}^\dagger \, \mathrm{e}^{-i\mathbf{q}\times\mathbf{r}} \right], \tag{4}$$

where

$$\Upsilon_{\mathbf{q}} = -i2\sqrt{\pi\lambda/\Xi} \left(\frac{\hbar^2}{2\hbar\omega_{\mathrm{LO}} m_e^*} \right)^{1/4} \frac{\hbar\omega_{\mathrm{LO}}}{\mathbf{q}}, \tag{5}$$

with $\vartheta_{\mathbf{q}}^\dagger/\vartheta_{\mathbf{q}}$ in eqn (5) representing the creation/annihilation operator, it is characterized by the physical quantities of the optic-phonon, including $\mathbf{r}$-position-vector, $\hbar\omega_{\mathrm{LO}}$-energy, and $\mathbf{q}$-wave-vector. In addition, Ξ is the volume; the el–op coupling constant in the GaSb/InAs, GaAs/AlAs, and GaN/AlN finite-square geometrical QWs is denoted by λ.

3. The core theoretical description for GaSb/InAs, GaAs/AlAs, and GaN/AlN finite-square geometrical QWs

In this section, the core theoretical description for heterostructures of GaSb/InAs, GaAs/AlAs, and GaN/AlN finite-square geometrical QWs is presented as below, where the magnetic field B in this formulation is oriented along the finite-square geometrical QW's z axis, while the charge carriers remain unrestricted within the (x, y) plane. Under these conditions, the quantized energy level $\mathcal{E}_{\ell,\mathcal{J}}$ and the associated wave function $\chi_{\ell,\mathcal{J}}$ are introduced as[25,26]

$$\chi_{\ell,\mathcal{J}} = {L_y}^{-1/2}\kappa_\ell(x - x_0)\mathrm{e}^{ik_y y}\Omega_{\mathcal{J}}(z), \tag{6}$$

in this description, the integer $\ell = 0,\ 1,\ 2,\ 3, \ldots$ enumerates the Landau-levels (LLs) in finite-square-geometrical QW, $\mathcal{J} = 0,\ 1,\ 2,\ 3, \ldots$ introduces the index of the corresponding sub-band-levels, and k_y is oriented along the finite-square geometrical QW's y axis for the wave-vector in GaSb/InAs, GaAs/AlAs, and GaN/AlN materials, the L_y normalization length. In the finite-square geometrical GaSb/InAs, GaAs/AlAs, and GaN/AlN QW, the function $\kappa_\ell(x - x_0)$ characterizes the harmonic oscillator with $x_0 = -{\Gamma}^2 k_y$. The parameter $\Gamma = (\hbar c/|e|B)^{1/2}$ designates the characteristic cyclotron-radius of the finite-square geometrical QW, where the quantity $\omega_c = B|e|/(m_e^*)$ specifies the corresponding cyclotron-frequency. In this core theoretical description, the finite-square geometrical potential QW $V(z)$ is examined in the following case:[27,28]

$$V(z) = \begin{cases} 0 \ \text{when} & |z| < L_W/2, \\ V_0 \ \text{when} & |z| > L_W/2, \end{cases} \tag{7}$$

here L_W specifies the thickness of the semiconductor layer that forms the quantum well. In a such $V(z)$ case, the energy symbol $\mathcal{E}_1$ of the lowest electric-sub-band in GaSb/InAs, GaAs/AlAs, and GaN/AlN finite-square geometrical QWs and the wave-function $\Omega_{\mathcal{J}}(z)$ is oriented along the z-axis are introduced as

$$\tan\left(\frac{\sqrt{2\mathcal{E}_1 m_{e1}^*}}{\hbar}\frac{L_W}{2}\right) = \left(\frac{(V_0 - \mathcal{E}_1)m_{e1}^*}{\mathcal{E}_1 m_{e2}^*}\right)^{1/2} \tag{8}$$

and

$$\Omega_1(z) = \begin{cases} A_0\cos(k_1 z), & |z| \le L_W/2, \\ B_0\exp[-k_2(|z| - L_W/2)], & |z| > L_W/2, \end{cases} \tag{9}$$

where $B_0 = A_0\cos(k_1 L_W/2)$, A_0 is the normalization constant, and $k_1 = \sqrt{2\mathcal{E}_1 m_{e1}^*}/\hbar$ and $k_2 = \sqrt{2(V_0 - \mathcal{E}_1)m_{e2}^*}/\hbar$ are the wave-vector in the GaSb/InAs, GaAs/AlAs, and GaN/AlN finite-square geometrical QWs. The effective-mass in the QW-material is m_{e1}^*, and in the QW-barrier material, it is m_{e2}^*.

4. The primary analytical findings concern the ELR in the GaSb/InAs, GaAs/AlAs, and GaN/AlN finite-depth-well confinement heterolayers

In this section, the primary analytical findings concern the hot-electron ELR in the GaSb/InAs, GaAs/AlAs, and GaN/AlN finite-depth-well confinement heterolayers are presented in a comprehensive and detailed way. Here, within the framework of the electron-temperature-based formalism for its energy relaxation dynamics, the analytic form for the electron energy-dissipation rate induced by electron–LO-phonon coupling *via* the Fröhlich interaction in the finite-square geometrical QWs can be established in the subsequent manner:

$$\begin{aligned} \mathrm{ELR} = {} & \frac{\mathcal{F}_{LO}\hbar\omega_{LO}{}^2 e^2}{N_e^S \xi^2 L_W}\left\{\exp\left(\frac{\Phi}{\mathcal{T}_\ell} - \frac{\Phi}{\mathcal{T}_e}\right) - 1\right\}\left(\frac{1}{\zeta_\infty} - \frac{1}{\zeta_0}\right) \times \sum_{\mathcal{J},\mathcal{J}'}\sum_{\ell,\ell'}\mathcal{F}\left(\mathcal{E}_{\ell,\mathcal{J}}, \mathcal{T}_e\right)\left[1 - \mathcal{F}\left(\mathcal{E}_{\ell,\mathcal{J}} + \hbar\omega_{LO}, \mathcal{T}_e\right)\right] \\ & \times \int_{-\infty}^{\infty} \mathrm{d}q_z \int_0^{\infty} \frac{\left|\mathcal{J}_{\ell,\ell'}(q_\perp)\right|^2 \left|\Theta_{\mathcal{J},\mathcal{J}'}(L_W q_z)\right|^2}{{q_\perp}^2 + {q_z}^2} q_\perp \mathrm{d}q_\perp \times \delta\left[\left(\ell' - \ell\right)\hbar\omega_c + \mathcal{E}_{\mathcal{J}}{}^{(z)}\left(V_0, L_W, m_1^*, m_2^*\right) - \hbar\omega_{LO}\right], \end{aligned} \tag{10}$$

here, N_e^S is the surface-carrier density, ζ_0 (ζ_∞) the static (frequency) dielectric constant in the GaSb/InAs, GaAs/AlAs, and GaN/AlN finite-depth-well confinement heterolayers, and e the electronic charge. Moreover, $\Phi = {k_B}^{-1}\hbar\omega_{LO}$ and $q_\perp = (q_x, q_y)$. The quantity $\left|\mathcal{J}_{\ell,\ell'}(q_\perp)\right|^2$ is introduced by

$$\begin{aligned} \left|\mathcal{J}_{\ell,\ell'}(q_\perp)\right|^2 = {} & (\ell_1!)^{-1}\ell_2!\left[\Gamma^2 {q_\perp}^2/2\right]^{\ell_1 - \ell_2}\mathrm{e}^{-\Gamma^2 {q_\perp}^2/2} \\ & \times \left[\Lambda_{\ell_2}{}^{\ell_1 - \ell_2}\left(\Gamma^2 {q_\perp}^2/2\right)\right]^2 \end{aligned} \tag{11}$$

here ℓ_1 and ℓ_2 are enumerated by $\max(\ell', \ell)$ and $\min(\ell', \ell)$, $\Lambda_{\ell_2}{}^{\ell_1 - \ell_2}(\Gamma^2 {q_\perp}^2/2)$ is the Laguerre-polynomial. Furthermore, the notation $\Theta_{\mathcal{J},\mathcal{J}'}(q_z)$ demonstrates the overlap integral induced by el–op coupling in the GaSb/InAs, GaAs/AlAs, and GaN/AlN finite-square geometrical QWs, takes the following formalism:

$$\Theta_{\mathcal{J},\mathcal{J}'}(L_W q_z) = \int_{-\infty}^{\infty} \Omega_{\mathcal{J}_i}^*(z)\ \mathrm{e}^{iq_z z}\Omega_{\mathcal{J}_f}(z)\mathrm{d}z, \tag{12}$$

where $\Omega_{\mathcal{J}_i}(z)$ and $\Omega_{\mathcal{J}_f}(z)$ are given within the specified formalism (9). Take note that Appendix A contains a detailed calculation of this overlap integral.

Next, we continue to make a comprehensive assessment of the $\Lambda_{\ell,\ell',\mathcal{J},\mathcal{J}'}(q_z, q_\perp)$ integral in eqn (10) to derive a clear formalism for the hot-electron ELR induced by el–op coupling in the GaSb/InAs, GaAs/AlAs, and GaN/AlN finite-square geometrical QWs, it adopts the form:

$$\Lambda_{\ell,\ell',\mathcal{J},\mathcal{J}'}(q_z,q_\perp)=\int_0^\infty q_\perp \mathrm{d}q_\perp \int_{-\infty}^{\infty}\frac{\left|\mathcal{J}_{\ell,\ell'}(q_\perp)\right|^2\left|\Theta_{\mathcal{J},\mathcal{J}'}(L_{\mathrm{W}}q_z)\right|^2}{{q_\perp}^2+{q_z}^2}\mathrm{d}q_z\times\delta\Big[\Big(\ell'-\ell\Big)\hbar\omega_{\mathrm{c}}+\mathcal{E}_{\mathcal{J}}{}^{(z)}\big(V_0,L_{\mathrm{W}},m_1^*,m_2^*\big)-\hbar\omega_{\mathrm{LO}}\Big]$$
$$=\int_{-\infty}^{\infty}\mathcal{I}_{\ell,\ell'}(q_\perp,q_z)\left|\Theta_{\mathcal{J},\mathcal{J}'}(L_{\mathrm{W}}q_z)\right|^2\mathrm{d}q_z\times\delta\Big[\Big(\ell'-\ell\Big)\hbar\omega_{\mathrm{c}}+\mathcal{E}_{\mathcal{J}}{}^{(z)}\big(V_0,L_{\mathrm{W}},m_1^*,m_2^*\big)-\hbar\omega_{\mathrm{LO}}\Big],\tag{13}$$

where

$$\mathcal{I}_{\ell,\ell'}(q_\perp,q_z)=\int_0^\infty q_\perp\frac{\left|\mathcal{J}_{\ell,\ell'}(q_\perp)\right|^2}{{q_\perp}^2+{q_z}^2}\mathrm{d}q_\perp.\tag{14}$$

We are aware that the Delta-Dirac function, $\delta[(\ell'-\ell)\hbar\omega_{\mathrm{c}}+\mathcal{E}_{\mathcal{J}}{}^{(z)}(V_0,L_{\mathrm{W}},m_1^*,m_2^*)-\hbar\omega_{\mathrm{LO}}]$, as shown by eqn (13), is independent of both q_z and $q_\perp$. As a result, the Lorentz function with the γ width can be used to approximate it as follows:

where, the formula of $\Theta_{\mathcal{J},\mathcal{J}'}(L_{\mathrm{W}}q_z)$ induced by el–op coupling in the GaSb/InAs, GaAs/AlAs, and GaN/AlN finite-square geometrical QWs is acquired for intrasubband transitions the subsequent manner:

$$\Theta_{1,1}(L_{\mathrm{W}}q_z)=2{A_0}^2\frac{\sin(q_zL_{\mathrm{W}}/2)}{2q_z}+\frac{1}{4}\Big[\frac{\sin[(2k_1+q_z)L_{\mathrm{W}}/2]}{2k_1+q_z}$$
$$+\frac{\sin[(2k_1-q_z)L_{\mathrm{W}}/2]}{2k_1-q_z}\Big]+\cos^2(L_Wk_1/2)$$
$$\times\left[\cos(q_zL_{\mathrm{W}}/2)\frac{2k_2}{4{k_2}^2+{q_z}^2}-\sin(q_zL_{\mathrm{W}}/2)\frac{q}{4{k_2}^2+{q_z}^2}\right]\Big\}\tag{18}$$

$$\delta\Big[\Big(\ell'-\ell\Big)\hbar\omega_{\mathrm{c}}+\mathcal{E}_{\mathcal{J}}{}^{(z)}\big(V_0,L_{\mathrm{W}},m_1^*,m_2^*\big)-\hbar\omega_{\mathrm{LO}}\Big]\approx L\Big\{\gamma,\Big[\Big(\ell'-\ell\Big)\hbar\omega_{\mathrm{c}}+\mathcal{E}_{\mathcal{J}}{}^{(z)}\big(V_0,L_{\mathrm{W}},m_1^*,m_2^*\big)-\hbar\omega_{LO}\Big]\Big\}$$
$$=2\gamma\Big/\pi\gamma^2+4\pi\Big[\Big(\ell'-\ell\Big)\hbar\omega_{\mathrm{c}}+\mathcal{E}_{\mathcal{J}}{}^{(z)}\big(V_0,L_{\mathrm{W}},m_1^*,m_2^*\big)-\hbar\omega_{\mathrm{LO}}\Big]^2.\tag{15}$$

Therefore, the formalism of the hot-electron ELR in the GaSb/InAs, GaAs/AlAs, and GaN/AlN finite-square geometrical QWs induced by el–op coupling in eqn (10) is rewritten in the subsequent manner:

Based on the acquired result of the analytical formulation governing the hot-electron ELR in the GaSb/InAs, GaAs/AlAs, and GaN/AlN finite-square geometrical QWs that are induced by the el–op interaction. We did extensive calculations and provided the findings derived from the numerical study in

$$\mathrm{ELR}=\frac{\mathcal{F}_{\mathrm{LO}}\hbar{\omega_{\mathrm{LO}}}^2e^2}{N_{\mathrm{e}}^{\mathrm{S}}\xi^2L_{\mathrm{W}}}\left\{\exp\left(\frac{\Phi}{\mathcal{T}_\ell}-\frac{\Phi}{\mathcal{T}_{\mathrm{e}}}\right)-1\right\}\left(\frac{1}{\zeta_\infty}-\frac{1}{\zeta_0}\right)\times\sum_{\mathcal{J},\mathcal{J}'}\sum_{\ell,\ell'}\mathcal{F}\big(\mathcal{E}_{\ell,\mathcal{J}},\mathcal{T}_{\mathrm{e}}\big)\big[1-\mathcal{F}\big(\mathcal{E}_{\ell,\mathcal{J}}+\hbar\omega_{\mathrm{LO}},\mathcal{T}_{\mathrm{e}}\big)\big]$$
$$\times2\gamma\Big/\left\{\pi\gamma^2+4\pi\Big[\Big(\ell'-\ell\Big)\hbar\omega_{\mathrm{c}}+\mathcal{E}_{\mathcal{J}}{}^{(z)}\big(V_0,L_{\mathrm{W}},m_1^*,m_2^*\big)-\hbar\omega_{\mathrm{LO}}\Big]^2\right\}\int_{-\infty}^{\infty}\mathcal{I}_{\ell,\ell'}(q_\perp,q_z)\left|\Theta_{\mathcal{J},\mathcal{J}'}(L_{\mathrm{W}}q_z)\right|^2\mathrm{d}q_z,\tag{16}$$

Following the systematic calculations, as shown in Appendix B. The expression of the ELR in the finite-square geometrical QW in formula (17) becomes

Section 5 in order to clarify how the hot-electron ELR responds to variation not only in the Landau-quantizing field, the well-

$$\mathrm{ELR}=\frac{\mathcal{F}_{\mathrm{LO}}\hbar{\omega_{\mathrm{LO}}}^2e^2}{N_{\mathrm{e}}^{\mathrm{S}}\xi^2L_{\mathrm{W}}}\left\{\exp\left(\frac{\Phi}{\mathcal{T}_\ell}-\frac{\Phi}{\mathcal{T}_{\mathrm{e}}}\right)-1\right\}\left(\frac{1}{\zeta_\infty}-\frac{1}{\zeta_0}\right)\times\sum_{\mathcal{J},\mathcal{J}'}\sum_{\ell,\ell'}\mathcal{F}\big(\mathcal{E}_{\ell,\mathcal{J}},\mathcal{T}_{\mathrm{e}}\big)\big[1-\mathcal{F}\big(\mathcal{E}_{\ell,\mathcal{J}}+\hbar\omega_{\mathrm{LO}},\mathcal{T}_{\mathrm{e}}\big)\big]$$
$$\times2\gamma\Big/\left\{\pi\gamma^2+4\pi\Big[\Big(\ell'-\ell\Big)\hbar\omega_{c}+\mathcal{E}_{\mathcal{J}}{}^{(z)}\big(V_0,L_{\mathrm{W}},m_1^*,m_2^*\big)-\hbar\omega_{\mathrm{LO}}\Big]^2\right\}\int_{-\infty}^{\infty}\exp\big(\Gamma^2{q_z}^2/2\big)\prod_{n+1}\big(\Gamma^2{q_z}^2/2\big)\times\Big|\Theta_{\mathcal{J},\mathcal{J}'}(L_{\mathrm{W}}q_z)\Big|^2\mathrm{d}q_z,\tag{17}$$

layer thickness, and the effective-carrier temperature, but also the surface-carrier density.

5. The results derived from the numerical study and the corresponding discussion

In this section, the results derived from the numerical study and the corresponding discussion are provided in detail, including (i) the comparison of how hot-electron ELR within the GaSb/InAs, GaAs/AlAs, and GaN/AlN finite-square geometrical QWs is impacted by the Landau-quantizing field, the well-layer thickness, the effective-carrier temperature, and the surface-carrier density; (ii) the acquired results of the finite-square geometrical QWs are comprehensively compared to those of the infinite-square geometrical QWs; (iii) the comprehensive discussion and succinct conclusion on the hot electron ELR within the GaSb/InAs, GaAs/AlAs, and GaN/AlN finite-square geometrical QWs are made in order to supplement valuable and practical findings for producing technologies of optoelectronic devices. The parameters of the GaSb/InAs, GaAs/AlAs, and GaN/AlN finite-square geometrical QWs used in this study are shown in Table 1. The figures below display the specific numerical findings:

In Fig. 1, we report a comparison highlighting the Landau-quantizing field-driven variations of hot-electron ELR owing to el–op coupling within GaSb/InAs, GaAs/AlAs, and GaN/AlN finite-and infinite-square geometrical QWs, as shown in corresponding Fig. 1c, b and a. Within our numerical analysis, the well-layer thickness ($L_W = 12$ nm), the surface-carrier density ($N_e^S = 2 \times 10^{15}$ m^{-2}), and the lattice ($T_\ell = 4.2$ K) and effective-carrier ($T_e = 300$ K) temperatures. We find resonant shifts among Landau levels that result in distinct resonance peaks when studying the electron within the GaSb/InAs, GaAs/AlAs, and GaN/AlN finite-square geometrical QWs that emits optical phonon. The phenomenon occurs specifically when the $\hbar\omega_{LO} = \ell\hbar\omega_c$ resonance-condition is met. This relationship can be expressed more explicitly as $\hbar\omega_{LO} = \ell\hbar|e|B/m_e^*$, emphasising the prerequisites for resonance. In this work, by employing Wolfram Mathematica software and the corresponding computation techniques, we determine the Landau quantizing field value when the Landau-level $\ell = 1$ corresponding to the GaSb/InAs, GaAs/AlAs, and GaN/AlN finite-square geometrical QWs are 12.09, 20.93, and 174.33 tesla. The Landau quantizing field values when $\ell = 2, 3, 4\ldots$ are determined similarly. In parallel, the corresponding resonance peaks to the Landau-level

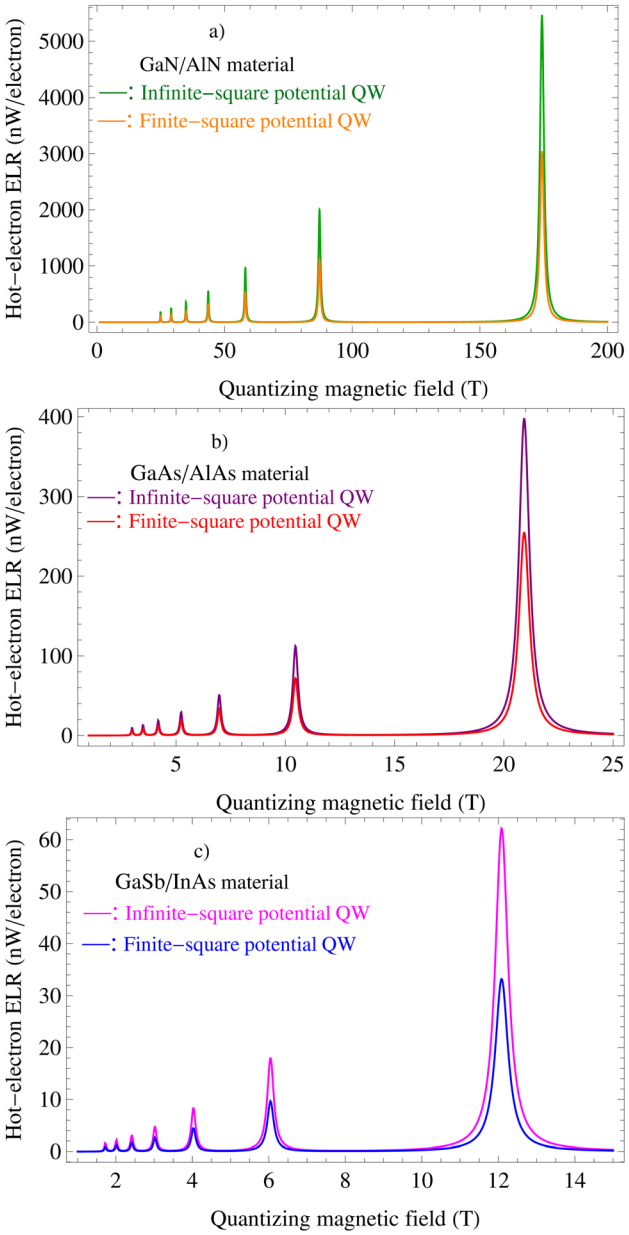

Fig. 1 A comparison highlighting the Landau-quantizing field-driven variations of hot-electron ELR owing to el–op coupling within the GaSb/InAs, GaAs/AlAs, and GaN/AlN finite-and infinite-square geometrical QWs, as shown in (a), (b), and (c), respectively. Within our numerical analysis, the well-layer thickness ($L_W = 12$ nm), the surface-carrier density ($N_e^S = 2 \times 10^{15}$ m^{-2}), and the lattice ($T_\ell = 4.2$ K) and effective-carrier ($T_e = 300$ K) temperatures.

Table 1 The parameters of the GaSb/InAs, GaAs/AlAs, and GaN/AlN finite-square geometrical QWs used in study[29–31]

Parameters	GaN	AlN	GaSb	InAs	GaAs	AlAs
$m_e^*(\times m_0)$	0.22	0.48	0.047	0.023	0.067	0.146
ζ_0	9.20	8.50	15.69	14.61	13.20	10.06
ζ_∞	5.35	4.77	14.44	11.8	10.89	8.16
$\hbar\omega_{LO}$ (meV)	91.83	113.0	29.8	30.2	36.25	50.09

$\ell = 1$ and Landau quantizing field 12.09, 20.93, and 174.33 tesla within GaSb/InAs, GaAs/AlAs, and GaN/AlN materials are applied to how the hot-electron ELR responds to variation not only in the effective-carrier temperature and the surface-carrier density but also the well-layer thickness. Within our numerical analysis, the hot-electron ELR GaSb/InAs, GaAs/AlAs, and GaN/AlN finite-square geometrical QWs shows a pronounced dependency on not only the effective-carrier temperature and the surface-carrier density but also the well-layer thickness. We

know that carriers in finite-square geometrical QWs experience resonant transitions between discrete Landau levels under a Landau quantizing field to quantise the electronic motion by absorbing or emitting an optic-phonon whose energy corresponds to the permitted separation of those states. In GaSb/InAs, GaAs/AlAs, and GaN/AlN finite-square QWs, the term for this phenomenon is the magnetophonon resonance (MPR) process, in which the phonon quantum precisely compensates for the difference between the initial and final electronic energies. The electron relaxation rate is a key metric for describing the cooling dynamics of hot carriers in GaSb/InAs, GaAs/AlAs, and GaN/AlN finite-square QWs. The characteristic timescale over which energetic electrons release phonons to dissipate their excess energy is reflected in this parameter. In GaSb/InAs, GaAs/AlAs, and GaN/AlN finite-square QWs, we observe a shorter relaxation time, which in turn increases the rate of carrier–phonon scattering. This increase results in noticeable resonant features in the electron–lattice relaxation spectrum when it's plotted against the Landau-quantizing field. The data shows differing scattering behaviors for GaSb/InAs, GaAs/AlAs, and GaN/AlN finite-square QWs, highlighting the variations in their optic-phonon energy intervals. Once the magnetic field is strong enough that the energy of the optic-phonons aligns with the gap between two LLs, the relaxation process hits its peak rate. This leads to fascinating differences in how electron-lattice relaxation behaves in the GaSb/InAs, GaAs/AlAs, and GaN/AlN materials. Each material showcases unique resonance features in this context, making for an interesting comparison. The figures indicate that the magnitude of the MPR oscillations in GaSb/InAs, GaAs/AlAs, and GaN/AlN finite-square geometrical QWs increases progressively as the Landau-quantizing field is strengthened. The resonance peak characteristics expand and attain higher amplitudes when subjected to stronger magnetic fields. Electronic relaxation processes that take place when the LL spacing becomes commensurate with the relevant phonon energy are responsible for the prominent maxima seen in these traces. The increase in the MPR amplitudes for materials like GaSb/InAs, GaAs/AlAs, and GaN/AlN finite-square geometrical QWs as the Landau-quantizing field strength rises is mainly due to the decrease in the magnetic length. Given that $\Gamma = \sqrt{\hbar c/(|e|B)}$, this characteristic length scale contracts with stronger Landau-quantizing fields, leading to a more pronounced oscillatory response. In particular, according to our findings, among the finite-square geometrical QW materials we examined, including GaSb/InAs, GaAs/AlAs, and GaN/AlN, the GaN/AlN-based finite-square geometrical QW exhibits the most robust hot-electron ELR response. Following closely behind is the GaAs/AlAs-based finite-square geometrical QW, which shows a diminished response, while the GaSb/InAs-based finite-square geometrical QW demonstrates the least dissipation of energy. Additionally, the findings presented here also reveal that the finite-square geometrical potential appreciably diminishes the hot-electron ELR response in the GaSb/InAs, GaAs/AlAs, and GaN/AlN QWs when compared to their infinite-square geometrical counterpart. This research paves the way for exciting advancements in optoelectronic devices that utilize finite-square geometrical QWs.

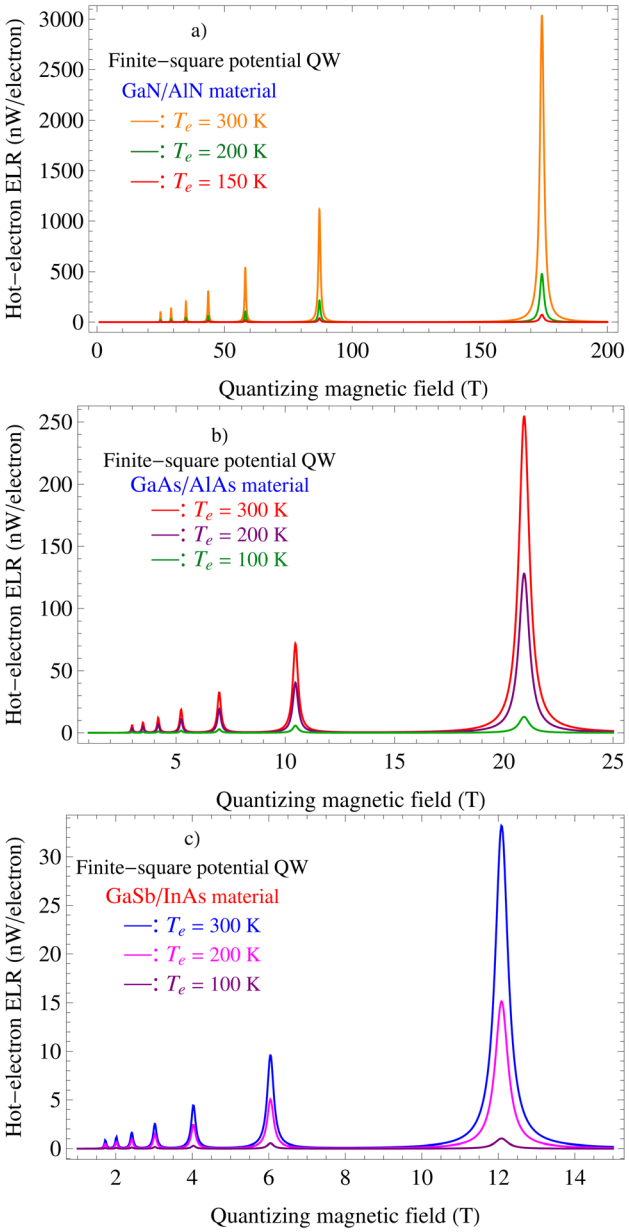

Fig. 2 A comparison exploring the Landau-quantizing field-driven changes of hot-electron ELR owing to el–op coupling within the GaSb/InAs, GaAs/AlAs, and GaN/AlN finite-square geometrical QWs for effective-carrier temperatures 300, 200, and 100 K, as shown in (a), (b) and (c), respectively. Within our numerical analysis, the well-layer thickness 12 nm, the surface-carrier density 2×10^{15} m^{-2}, and the lattice's temperature 4.2 K.

Fig. 2 displays our numerical findings for a comparison exploring the Landau-quantizing field-driven changes of hot-electron ELR owing to el–op coupling within the GaSb/InAs, GaAs/AlAs, and GaN/AlN finite-square geometrical QWs for effective-carrier temperatures 300, 200, and 100 K. Within our numerical analysis, the well-layer thickness is 12 nm, the surface carrier density 2×10^{15} m^{-2}, and the lattice's

temperature 4.2 K. Noting that the characteristics of GaSb/InAs, GaAs/AlAs, and GaN/AlN materials owing to the effective-carrier temperature driven changes are described in Fig. 2c, b and a, respectively. According to our findings, the hot-electron ELR within the GaSb/InAs, GaAs/AlAs, and GaN/AlN finite-square geometrical QWs is appreciably impacted by effective-carrier temperatures on both the MPR peak's broadening and intensity. Concretely, the greater the increment of the effective-carrier temperature is, the more enhanced the MPR peak's broadening and intensity induced by el–op coupling will be. This characteristic is found in the Landau-quantising field-driven variations of hot-electron ELR within GaSb/InAs, GaAs/AlAs, and GaN/AlN finite-square geometrical QWs in corresponding Fig. 2c, b and a. Additionally, our findings within the finite-square geometrical QW materials show that as the effective-carrier temperature is enhanced from $100 to $200 and then to $300 K, we observe distinct shifts in both the MPR peak's broadening and intensity for the hot-electron ELR in the finite-square geometrical QWs, which are unique to each GaSb/InAs, GaAs/AlAs, and GaN/AlN material. The differences observed stem from the el–op interaction within GaSb/InAs, GaAs/AlAs, and GaN/AlN finite-square geometrical QWs. This interaction alters the strengths of el–ph coupling, ultimately affecting the hot-electron ELR spectrum. The different thermal behaviors seen in various compounds are tied to their scattering phase space, phonon dispersions, and the changes in transition probabilities due to quantum-confinement. Understanding these patterns is crucial for choosing the right barrier combinations to enhance performance in quantum-information and optoelectronic systems based on QW, especially where managing hot-electron ELR is key to optimizing devices. The results we've gathered indicate that changes in the electronic effective temperature—ranging from 100 to 200 and up to 300 K—do not impact the positions of the magneto-phonon resonance oscillation peaks in systems like GaSb/InAs, GaAs/AlAs, and GaN/AlN finite-square geometrical QWs. This finding offers valuable insights that could be leveraged in the development and refinement of optoelectronic devices.

We present our numerical finding in Fig. 3, which is a comparison exploring the effective-carrier temperature-driven variations of hot-electron ELR owing to el–op coupling within the GaSb/InAs, GaAs/AlAs, and GaN/AlN finite-and infinite-square geometrical QWs. Within our numerical analysis, the

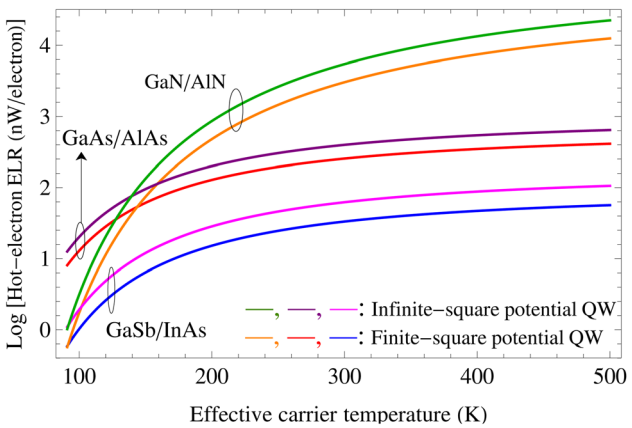

Fig. 3 A comparison exploring the effective-carrier temperature-driven variations of hot-electron ELR owing to el–op coupling within the GaSb/InAs, GaAs/AlAs, and GaN/AlN finite-and infinite-square geometrical QWs. Within our numerical analysis, the well-layer thickness is 12 nm, the surface-carrier density 2×10^{15} m^{-2}, the Landau-quantizing field 12.09, 20.93, and 174.33 T for GaSb/InAs, GaAs/AlAs, and GaN/AlN materials, and the lattice's temperature 4.2 K.

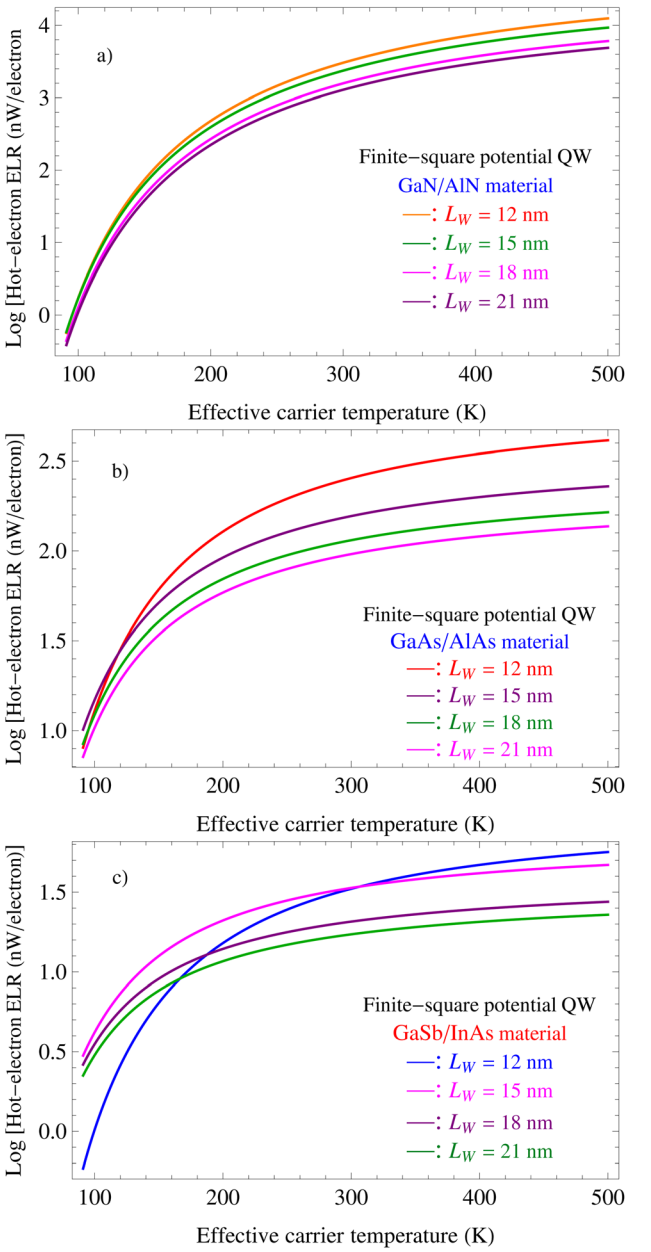

Fig. 4 A comparison highlighting the effective-carrier temperature-driven variations of hot-electron ELR owing to el–op coupling within the GaSb/InAs, GaAs/AlAs, and GaN/AlN finite-square geometrical QWs for the well-layer thicknesses are 12, 15, 18, and 21 nm, as shown in (a), (b) and (c), respectively. Within our numerical analysis, the surface-carrier density 2×10^{15} m^{-2}, the Landau-quantizing field 12.09, 20.93, and 174.33 T for GaSb/InAs, GaAs/AlAs, and GaN/AlN materials, the lattice's temperature 4.2 K.

well-layer thickness is 12 nm, the surface-carrier density 2×10^{15} m^{-2}, the Landau-quantizing field 12.09, 20.93, and 174.33 T for GaSb/InAs, GaAs/AlAs, and GaN/AlN materials, and the lattice's temperature 4.2 K. A closer look reveals that the response of the ELR to the effective-carrier temperature-driven increments varies significantly among GaSb/InAs, GaAs/AlAs, and GaN/AlN materials. Notably, the hot-electron ELR within the GaN/AlN finite-and infinite-square geometrical QWs demonstrates that this material has the most appreciable augmentation with the effective-carrier temperature-driven increments, followed by GaAs/AlAs, and the least, GaSb/InAs material. The order of energy relaxation rates is largely determined by the specific phonon characteristics of the materials and how well carriers interact with the lattice in the respective QWs. In the case of the GaN/AlN finite- and infinite-square geometrical QW heterostructures, energy dissipation occurs at a notably rapid pace. This is primarily because the relevant optic phonons possess significant energy values, and the material's strong ionic nature enhances the long-range coupling between electrons and phonons. Furthermore, the pronounced dielectric contrast at the interfaces gives rise to effective phonon modes that promote quicker cooling of hot carriers. On the other hand, for the GaAs/AlAs finite- and infinite-square geometrical QWs, both the energy scale of the phonons and the strength of their coupling are lower in comparison to GaN/AlN finite-and infinite-square potential QW heterostructures, resulting in a moderate energy relaxation rate. When considering the GaSb/InAs heterostructures, it exhibits the least energy loss since its optic phonons are less energetic, and the polar interactions are weaker. Additionally, the staggered band alignment in GaSb/InAs finite-and infinite-square geometrical QWs relocates electronic states further from the interfaces, reducing their engagement with phonon modes associated with the interfaces. These factors together result in a clear trend of decreasing energy relaxation rates from GaN/AlN to GaSb/InAs finite- and infinite-square potential QW heterostructures. Moreover, the findings obtained for GaSb/InAs, GaAs/AlAs, and GaN/AlN finite-square geometrical QW materials when the effective-carrier temperature $\mathcal{T}_e > 120$ K show that the GaN/AlN material not only has the highest magnitude but also the fastest increase in the ELR. The GaAs/AlAs material follows, while the GaSb/InAs material shows the lowest values and the least temperature dependency. Nevertheless, when the effective-carrier temperature $\mathcal{T}_e < 120$ K, according to the findings showed in Fig. 3, the hot-electron ELR displays that GaAs/AlAs finite- and infinite-square geometrical QW material has the highest magnitude among GaN/AlN, GaAs/AlAs, and GaSb/InAs materials.

In Fig. 4, we provide in detail a comparison highlighting the effective-carrier temperature-driven variations of hot-electron ELR owing to el–op coupling within the GaSb/InAs, GaAs/AlAs, and GaN/AlN finite-square geometrical QWs for the well-layer thicknesses are 12, 15, 18, and 21 nm. Within our numerical analysis, the surface-carrier density 2×10^{15} m^{-2}, the Landau-quantizing field 12.09, 20.93, and 174.33 T for GaSb/InAs, GaAs/AlAs, and GaN/AlN materials, the lattice's temperature 4.2 K. The findings shown in Fig. 4 unequivocally describe an increased hot-electron ELR within the GaSb/InAs, GaAs/AlAs, and GaN/AlN finite-square geometrical QWs with the effective-carrier temperature-driven increments for the well-layer thicknesses, including 12, 15, 18, and 21 nm. The findings suggest that the rate of energy dissipation by carriers in layers of the GaAs/AlAs and GaN/AlN finite-square geometrical QWs changes in a systematic way as the effective-carrier temperature varies under different well-layer thickness conditions. In particular, in Fig. 4, the findings unequivocally prove that there is a decreased hot-electron ELR within the GaSb/InAs, GaAs/AlAs, and GaN/AlN finite-square geometrical QWs with the well-layer thickness-driven increments from 12 nm to 21 nm. Nevertheless, for the GaSb/InAs material of the finite-square geometrical QW, the decreased hot-electron ELR within the effective-carrier temperature-driven variations when the well-layer thickness driven increments are from 12 nm to 21 nm is complicated when $\mathcal{T}_e < 300$ K, especially in the well-layer thickness 12 nm case. The findings of this study provide a qualitative basis that helps pinpoint appropriate material systems to boost the efficiency and performance of optoelectronic components and upcoming quantum-technology platforms.

We provide our numerical findings in Fig. 5 for a comparison exploring the well-layer thickness-driven changes of hot-electron ELR owing to el–op coupling within the GaSb/InAs, GaAs/AlAs, and GaN/AlN finite-and infinite-square geometrical QWs. Within our numerical analysis, the effective-carrier temperature is 300 K, the surface-carrier density 2×10^{15} m^{-2}, the Landau-quantizing field 12.09, 20.93, and 174.33 T for GaSb/InAs, GaAs/AlAs, and GaN/AlN materials, and the lattice's temperature 4.2 K. Our numerical analysis unequivocally proves that the diminishment of the hot-electron ELR to the well-layer thickness-driven increments varies significantly among GaSb/InAs, GaAs/AlAs, and GaN/AlN materials. Notably, the hot-electron ELR within the GaN/AlN finite- and infinite-square geometrical QW material demonstrates that this material has the most appreciable diminishment rate with the well-layer

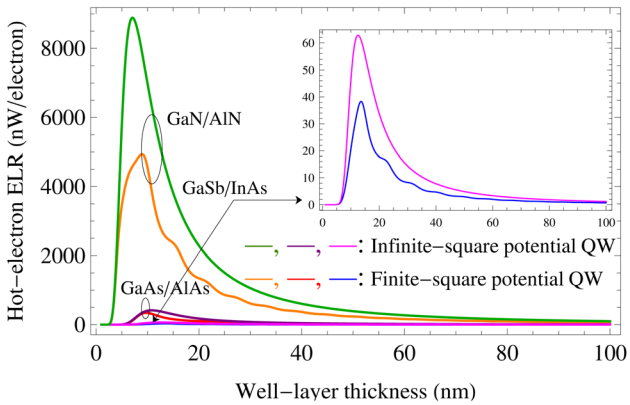

Fig. 5 A comparison exploring the well-layer thickness-driven changes of hot-electron ELR owing to el–op coupling within the GaSb/InAs, GaAs/AlAs, and GaN/AlN finite-and infinite-square geometrical QWs. Within our numerical analysis, the effective-carrier temperature is 300 K, the surface-carrier density 2×10^{15} m^{-2}, the Landau-quantizing field 12.09, 20.93, and 174.33 T for GaSb/InAs, GaAs/AlAs, and GaN/AlN materials, and the lattice's temperature 4.2 K.

thickness driven increments when L_W > 10 nm, followed by GaAs/AlAs, and the least, GaSb/InAs material. Simultaneously, the computed findings further prove that the reduced hot-electron energy-loss rate induced by the finite square confinement geometrical potential in GaN/AlN, GaAs/AlAs, and GaSb/InAs nanostructured materials is appreciable.

The findings revealed in Fig. 6 unequivocally show a comparison exploring the Landau-quantizing field-driven changes of hot-electron ELR owing to el–op coupling within the GaSb/InAs, GaAs/AlAs, and GaN/AlN finite-square geometrical QWs for the surface-carrier densities 2×10^{15}, 5×10^{15}, and 8×10^{15} m^{-2}. Within our numerical analysis, the well-layer thickness is 12 nm, the effective-carrier temperatures 300 K, and the lattice's temperature 4.2 K. Our numerical analysis in this work unequivocally proves that the decrement of the hot-electron ELR to the surface-carrier density-driven increments in all GaSb/InAs, GaAs/AlAs, and GaN/AlN nanomaterials. In more detail, when the surface-carrier density within the GaSb/InAs, GaAs/AlAs, and GaN/AlN finite-square geometrical QWs augments from 2×10^{15} to 5×10^{15} and to 8×10^{15} m^{-2}, the hot-electron ELR within the GaSb/InAs, GaAs/AlAs, and GaN/AlN material is appreciably impacted on both its peak's broadening and intensity, as reported in corresponding Fig. 6c, b and a. More concretely, according to our findings, the greater the increment of the surface-carrier density is, the more diminished the MPR peak's broadening and intensity induced by el–op coupling will be. Simultaneously, this characteristic will be appreciably proved in the surface-carrier-density-driven variations of hot-electron ELR within GaSb/InAs, GaAs/AlAs, and GaN/AlN finite-square geometrical QWs in the corresponding Fig. 7. Besides, our research on finite-square geometrical QW materials reveals that increasing the surface-carrier density from 2×10^{15} to 5×10^{15} and then to 8×10^{15} m^{-2} leads to noticeable changes in both the broadening and intensity of the MPR peak for the hot-electron ELR. These variations are distinct for each material, including GaSb/InAs, GaAs/AlAs, and GaN/AlN. This feature of GaSb/InAs, GaAs/AlAs, and GaN/AlN finite-square geometrical QW materials are also appreciably understood in the Fig. 7. Our comparative analysis provides a solid foundation for selecting materials and optimising structures in the pursuit of high-performance optoelectronic devices operating in the ultraviolet, infrared, and terahertz ranges.

Finally, in order to demonstrate the appreciable differences in the hot-electron ELR between the GaSb/InAs, GaAs/AlAs, and

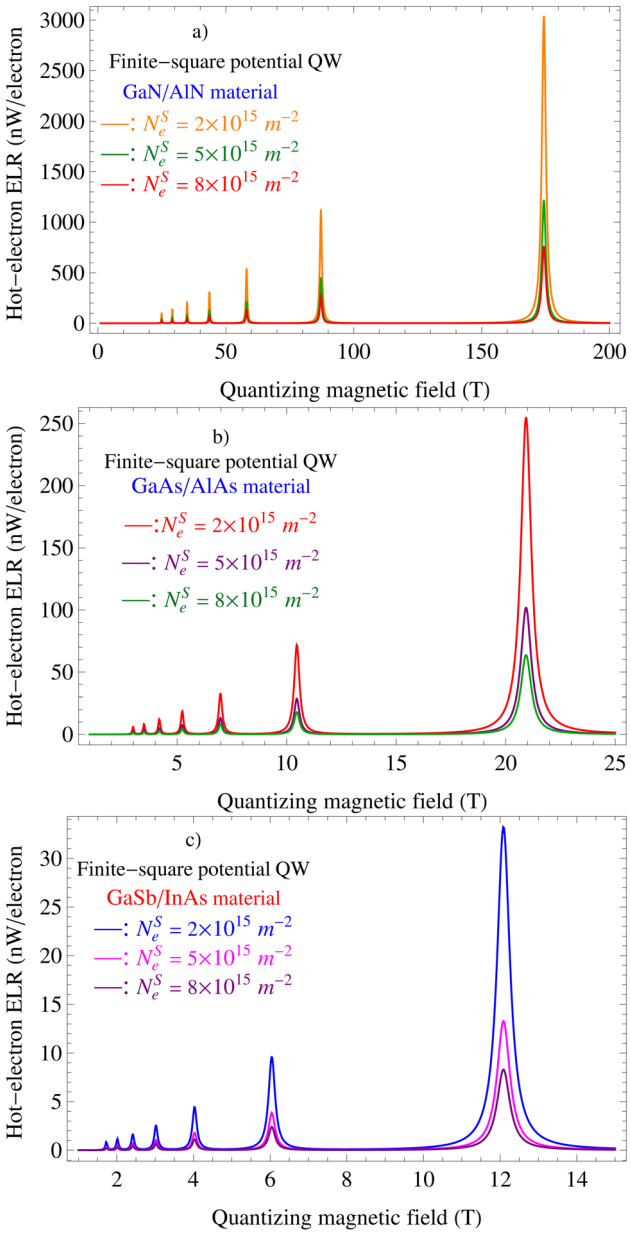

Fig. 6 A comparison exploring the Landau-quantizing field-driven changes of hot-electron ELR owing to el–op coupling within the GaSb/InAs, GaAs/AlAs, and GaN/AlN finite-square geometrical QWs for the surface-carrier densities 2×10^{15}, 5×10^{15}, and 8×10^{15} m^{-2}, as shown in (a), (b) and (c), respectively. Within our numerical analysis, the well-layer thickness is 12 nm, the effective-carrier temperatures 300 K, and the lattice's temperature 4.2 K.

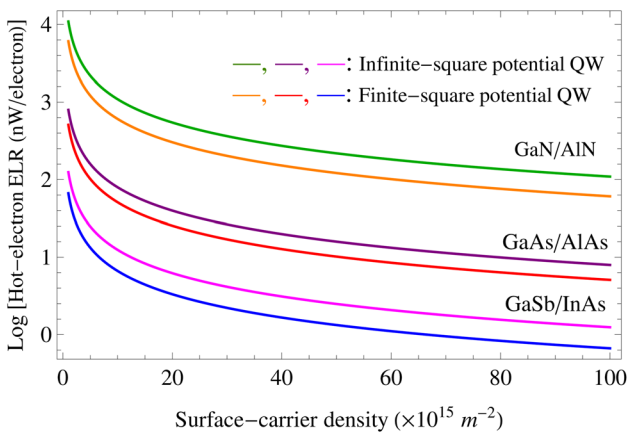

Fig. 7 A comparison exploring the surface-carrier density-driven changes of hot-electron ELR owing to el–op coupling within the GaSb/InAs, GaAs/AlAs, and GaN/AlN finite-and infinite-square geometrical QWs. Within our numerical analysis, the well-layer thickness 12 nm, the effective-carrier temperature 300 K, the Landau-quantizing field 12.09, 20.93, and 174.33 T for GaSb/InAs, GaAs/AlAs, and GaN/AlN materials, and the lattice's temperature 4.2 K.

GaN/AlN QW materials due to the surface-carrier-density-driven variations for both finite- and infinite-square geometrical potentials, we provided the numerical findings for a comparison exploring the surface-carrier-density-driven changes of hot-electron ELR owing to el–op coupling within the GaSb/InAs, GaAs/AlAs, and GaN/AlN finite- and infinite-square geometrical QWs. Within our numerical analysis, the well-layer thickness is 12 nm, the effective-carrier temperature 300 K, the Landau quantizing field 12.09, 20.93, and 174.33 T for GaSb/InAs, GaAs/AlAs, and GaN/AlN materials, and the lattice's temperature 4.2 K in Fig. 7. Our data reveals that the response of the ELR to the surface-carrier-density-driven increments is significantly different among GaSb/InAs, GaAs/AlAs, and GaN/AlN materials for both finite- and infinite-square geometrical QWs. Concretely, the hot-electron ELR within the GaN/AlN has the most appreciable value and dependence on the surface-carrier-density-driven increments, followed by GaAs/AlAs, and the least, GaSb/InAs QW for both finite- and infinite-square geometrical potentials. This outcome stems from the fundamental differences in phonon characteristics and the ways electrons interact with phonons within the three types of heterostructures. GaN/AlN stands out with the highest hot-electron ELR, thanks to its elevated LO-phonon energy and strong polar attributes. These factors greatly enhance the Fröhlich-type interaction between electrons and phonons, allowing for efficient energy dissipation during each scattering event. The significant dielectric mismatch further amplifies this effect, resulting in strong relaxation facilitated by interface phonons. On the other hand, GaAs/AlAs showcases average phonon energy and polarity, leading to a moderate interaction strength and an ELR that falls between the two extremes. In contrast, GaSb/InAs demonstrates the lowest ELR due to its reduced optical phonon energy and a weaker polar interaction. Additionally, the type-II band alignment in GaSb/InAs effectively separates electrons from the interfaces, limiting their interaction with interface phonon modes. Consequently, the hot-electron energy relaxation rate exhibits a consistent decline from GaN/AlN to GaSb/InAs. Recognizing such GaSb/InAs, GaAs/AlAs, and GaN/AlN material characteristics and finite- and infinite-square geometrical confinement potentials is essential for selecting the appropriate barrier combination and materials that can boost performance in quantum-information and optoelectronic systems utilizing QWs. This is particularly important when it comes to managing hot-electron ELR, which is vital for optimizing device functionality.

6. Conclusions

This work investigates the hot-electron ELR in GaSb/InAs, GaAs/AlAs, and GaN/AlN finite-square geometrical QWs, considering e–LO-ph coupling *via* the Fröhlich interaction within an electron-temperature framework. The results are summarized as follows: (i) the MPR oscillation amplitudes within GaSb/InAs, GaAs/AlAs, and GaN/AlN finite-square geometrical QWs are markedly enhanced by a stronger magnetic field. (ii) The ELR within all GaSb/InAs, GaAs/AlAs, and GaN/AlN finite-square geometrical QWs owing to e–LO-ph coupling augments as the effective-carrier temperature augments, whereas it diminishes as the well-layer thickness and surface-carrier density are enhanced. (iii) The ELR within the GaSb/InAs, GaN/AlN, and GaAs/AlAs QW heterostructures is appreciably impacted by quantum confinement potentials on both the strength and amplitude of the MPR oscillation peak. Concretely, the finite-square geometrical potential appreciably diminishes the hot-electron ELR response within the GaSb/InAs, GaAs/AlAs, and GaN/AlN QWs when compared to their infinite-square geometrical counterparts; this highlights the important role of quantum confinement engineering in controlling 2D electronic energy relaxation. (iv) When the well-layer thickness of QWs is sufficiently small, the quantum confinement potential influence on the hot-electron ELR becomes highly sensitive. (v) The response of the ELR to the variations of the effective-carrier temperature, the well-layer thickness, and the surface-carrier density is appreciably different among GaSb/InAs, GaAs/AlAs, and GaN/AlN quantum well materials. Notably, the ELR within the GaN/AlN material has the most appreciable value, followed by GaAs/AlAs, and the least, GaSb/InAs material. (vi) These material-dependent variations in ELR provide a useful basis for selecting QW systems for optoelectronic applications, where GaN/AlN favors efficient energy dissipation, GaSb/InAs supports slower carrier cooling, and GaAs/AlAs offers a balance between relaxation and carrier retention. (vii) The reduced ELR in finite quantum wells enhances the hot-electron lifetime and phase coherence, highlighting the importance of confinement engineering as an effective tool for controlling energy relaxation and optimizing device-relevant properties. Taken together, the present results indicate that finite square geometrical confinement can serve as an effective means to control hot-electron energy relaxation in semiconductor heterostructures. This effect may have direct implications for high-power electronics (GaN/AlN), infrared optoelectronic devices (GaAs/AlAs), and mid-infrared or narrow-bandgap systems (GaSb/InAs), where hot-carrier dynamics play a central role in determining transport and response characteristics.

Conflicts of interest

There are no conflicts to declare.

Data availability

The authors confirm that the data supporting the findings of this study are available within the article.

A Appendices

A.1 Appendix A

Now the overlap integral induced by the el–op coupling in finite-square geometrical QWs in eqn (12) is comprehensively evaluated using the subsequent procedures:

Firstly, in the finite-square QWs the normalization constant A_0 is thoroughly determined *via* the subsequent normalization condition

$$\int_{-\infty}^{\infty} |\Omega_1(z)|^2 \mathrm{d}z = 2\int_0^{\infty} |\Omega_1(z)|^2 \mathrm{d}z = 1, \tag{A.1}$$

we have

$$\begin{aligned}\int_0^{\infty} |\Omega_1(z)|^2 \mathrm{d}z &= \int_0^{L_W/2} {A_0}^2 \cos^2(k_1 z)\mathrm{d}z + \int_{L_W/2}^{\infty} {B_0}^2 \, \mathrm{e}^{-2k_2(z-L_W/2)}\mathrm{d}z \\ &= {A_0}^2 \int_0^{L_W/2} \frac{1+\cos(2k_1 z)}{2}\mathrm{d}z + {B_0}^2 \int_0^{\infty} \mathrm{e}^{-2k_2 v}\mathrm{d}v \\ &= \frac{1}{2}\left[\frac{{A_0}^2 L_W}{2} + \frac{{A_0}^2 \sin(L_W k_1)}{2k_1} + \frac{{B_0}^2}{k_2}\right],\end{aligned} \tag{A.2}$$

ultimately, we were able to derive the following equation for the normalisation constant A_0:

$${A_0}^{-2} = \frac{L_W}{2} + \frac{\sin(L_W k_1)}{2k_1} + \frac{\cos^2(L_W k_1/2)}{k_2}. \tag{A.3}$$

Secondly, the subsequent calculations are for the overlap integral induced by el–op coupling in the GaSb/InAs, GaAs/AlAs, and GaN/AlN finite-square geometrical QWs:

$$\begin{aligned}\Theta_{1,1}(L_W q_z) &= \int_{-\infty}^{\infty} \Omega_1^*(z) \, \mathrm{e}^{iq_z z}\Omega_1(z)\mathrm{d}z \\ &= 2\int_0^{\infty} |\Omega_1|^2 \cos(q_z z)\mathrm{d}z \\ &= 2{A_0}^2\left[\Theta_{1,1}^{\mathrm{in}}(L_W q_z) + \Theta_{1,1}^{\mathrm{out}}(L_W q_z)\right],\end{aligned} \tag{A.4}$$

where the superscripts in and out refer to the inner and outer regions of the GaSb/InAs, GaAs/AlAs, and GaN/AlN finite-square geometrical QWs. It means that symbols $\Theta_{1,1}^{\mathrm{in}}(L_W q_z)$ and $\Theta_{1,1}^{\mathrm{out}}(L_W q_z)$ are the integrals induced by el–op coupling at the finite-square geometrical QW inner and outer regions, and they take the subsequent form

$$\Theta_{1,1}^{\mathrm{in}}(L_W q_z) = \int_0^{L_W/2} \cos^2(k_1 z)\cos(q_z z)\mathrm{d}z \tag{A.5}$$

and

$$\Theta_{1,1}^{\mathrm{out}}(L_W q_z) = \cos^2\left(\frac{L_W k_1}{2}\right) \times \int_0^{\infty} \mathrm{e}^{-2k_2 v}\cos[q_z(v + L_W/2)]\mathrm{d}v. \tag{A.6}$$

An extensive evaluation for $\Theta_{1,1}^{\mathrm{in}}(L_W q_z)$ is provided below:

$$\begin{aligned}\Theta_{1,1}^{\mathrm{in}}(L_W q_z) &= \int_0^{L_W/2} \cos^2(k_1 z)\cos(q_z z)\mathrm{d}z \\ &= \frac{1}{2}\int_0^{L_W/2} \cos(q_z z)\mathrm{d}z + \frac{1}{2}\int_0^{L_W/2} \cos(2k_1 z)\cos(q_z z)\mathrm{d}z \\ &= \frac{\sin(q_z L_W/2)}{2q_z} + \frac{1}{4}\left[\frac{\sin[(2k_1+q_z)L_W/2]}{2k_1+q_z} + \frac{\sin[(2k_1-q_z)L_W/2]}{2k_1-q_z}\right].\end{aligned} \tag{A.7}$$

The following is a thorough evaluation for $\Theta_{1,1}^{\mathrm{out}}(L_W q_z)$, in which we set $v = z - L_W/2$:

$$\begin{aligned}\Theta_{1,1}^{\mathrm{out}}(L_W q_z) &= \cos^2(L_W k_1/2)\int_0^{\infty} \mathrm{e}^{-2k_2 v}\cos[q_z(v + L_W/2)]\mathrm{d}v \\ &= \cos^2(L_W k_1/2)[\cos(q_z L_W/2) \times \int_0^{\infty} \mathrm{e}^{-2k_2 v}\cos(q_z v)\mathrm{d}v \\ &\quad -\sin(q_z L_W/2)\int_0^{\infty} \mathrm{e}^{-2k_2 v}\sin(q_z v)\mathrm{d}v\Big].\end{aligned} \tag{A.8}$$

By using two common Laplace-type integrals,[32] they are given as

$$\int_0^{\infty} \exp(-cx)\cos(\mathrm{d}x)\mathrm{d}x = \frac{c}{c^2+d^2}, \tag{A.9a}$$

$$\int_0^{\infty} \exp(-cx)\sin(\mathrm{d}x)\mathrm{d}x = \frac{d}{c^2+d^2}, \tag{A.10a}$$

We derive the following results:

$$\int_0^{\infty} \mathrm{e}^{-2k_2 v}\cos(q_z v)\mathrm{d}v = \frac{2k_2}{4{k_2}^2 + {q_z}^2}, \tag{A.11}$$

$$\int_0^{\infty} \mathrm{e}^{-2k_2 v}\sin(q_z v)\mathrm{d}v = \frac{q_z}{4{k_2}^2 + {q_z}^2}. \tag{A.12}$$

Ultimately, we were able to derive the subsequent equation for the $\Theta_{1,1}^{\mathrm{out}}(q_z)$ integral:

$$\begin{aligned}\Theta_{1,1}^{\mathrm{out}}(L_W q_z) &= \cos^2(L_W k_1/2) \times \left[\cos(q_z L_W/2)\frac{2k_2}{4{k_2}^2 + {q_2}^2}\right. \\ &\quad \left. - \sin(q_z L_W/2)\frac{q_z}{4{k_2}^2 + {q_2}^2}\right].\end{aligned} \tag{A.13}$$

By submitting eqn (A.7) and (A.13) into (A.4), we obtain the comprehensive result for the overlap integral induced by el–op coupling in the GaSb/InAs, GaAs/AlAs, and GaN/AlN finite-square geometrical QWs:

$$\begin{aligned}\Theta_{1,1}(L_W q_z) &= 2{A_0}^2\frac{\sin(q_z L_W/2)}{2q_z} + \frac{1}{4}[\frac{\sin[(2k_1+q_z)L_W/2]}{2k_1+q_z} \\ &\quad + \frac{\sin[(2k_1-q_z)L_W/2]}{2k_1-q_z}] + \cos^2(L_W k_1/2) \\ &\quad \times \left[\cos(q_z L_W/2)\frac{2k_2}{4{k_2}^2 + {q_2}^2} - \sin(q_z L_W/2)\frac{q}{4{k_2}^2 + {q_2}^2}\right]\Big\}\end{aligned} \tag{A.14}$$

A.2 Appendix B

We now consider the subsequent $\mathcal{I}_{\ell,\ell'}(q_\perp, q_z)$ integral in eqn (14) in great detail in the case where $\ell = 0$, we have

$$\mathcal{I}_{\ell,\ell'}(q_\perp,q_z)\equiv\mathcal{I}_{0,\ell'}(q_\perp,q_z)=\int_0^\infty q_\perp\frac{\left|\mathcal{J}_{0,\ell'}(\Gamma q_\perp)\right|^2}{{q_\perp}^2+{q_z}^2}\mathrm{d}q_\perp$$
$$=\frac{1}{\ell'!}\int_0^\infty\frac{\left[(\Gamma q_\perp)^2\right]^{\ell'}\exp\left[-(\Gamma q_\perp)^2/2\right]}{{q_\perp}^2+{q_z}^2}q_\perp\mathrm{d}q_\perp. \quad \text{(B.1)}$$

Setting $t=\Gamma^2{q_\perp}^2/2\rightarrow{q_\perp}^2=2t/\Gamma^2$, $q_\perp\mathrm{d}q_\perp=dt/\Gamma^2$. Then, we obtain

$$\mathcal{I}_{\ell,\ell'}(q_\perp,q_z)=\frac{1}{\ell'!}\int_0^\infty\frac{t^{\ell'}\exp(-t)}{2t/\Gamma^2+{q_2}^2}\times\frac{\mathrm{d}t}{\Gamma^2}$$
$$=\frac{1}{\ell'!}\int_0^\infty\frac{t^{\ell'}\exp(-t)}{2t+(q_z)^2}\mathrm{d}t \quad \text{(B.2)}$$
$$=\frac{1}{2}\exp\left(\Gamma^2{q_2}^2/2\right)\prod_{n+1}\left(\Gamma^2{q_2}^2/2\right),$$

where $\prod(x)=\int_1^\infty\exp(-xt)/t^n\mathrm{d}t$ is the generalized exponential integral.[n]

References

1 Y. Gu, Y. s. Liu, G. Yang, F. Xie, C. Zhu, Y. Yu, X. Zhang, N. Lu, Y. Wang and G. Chen, *Nanoscale Adv.*, 2021, **3**, 2649–2656.
2 T. C. Phong, L. N. Minh and N. D. Hien, *Nanoscale Adv.*, 2024, **6**, 832–845.
3 H. K. Dan, P. T. Vinh and N. D. Hien, *Nanoscale Adv.*, 2024, **6**, 6253–6264.
4 N. T. Thuy and N. D. Hien, *Nanoscale Adv.*, 2025, **7**, 1234–1245.
5 N. T. Thuy and N. D. Hien, *Nanoscale Adv.*, 2025, **7**, 6789–6798.
6 S. Tiraş, A. Das and S. Rastegar, *Phys. E*, 2013, **50**, 1–8.
7 I. Makhfudz, N. Cavassilas, M. Giteau, H. Esmaielpour, D. Suchet, A.-M. Daré and F. Michelini, *J. Phys. D: Appl. Phys.*, 2022, **55**, 475102.
8 I. Makhfudz, N. Cavassilas, Y. Hajati, H. Esmaielpour and F. Michelini, *Phys. Rev. Appl.*, 2023, **19**, 044002.
9 S. Arshia Khatoon, M. Ansari, S. S. Z. Ashraf and M. Obaidurrahman, *J. Appl. Phys.*, 2021, **129**, 014308.
10 F. C. M. Spoor, S. Tomić, A. J. Houtepen and L. D. A. Siebbeles, *ACS Nano*, 2017, **11**, 6286–6294.
11 J. Shah, A. Pinczuk, A. C. Gossard and W. Wiegmann, *Phys. Rev. Lett.*, 1985, **54**, 2045.
12 C. H. Yang, J. M. Carlson-Swindle, S. A. Lyon and J. M. Worlock, *Phys. Rev. Lett.*, 1985, **55**, 2359.
13 S. Rudin and T. L. Reinecke, *Phys. Rev. B: Condens. Matter Mater. Phys.*, 1990, **41**, 7713–7717.
14 S. Das Sarma and J. Campos, *Phys. Rev. B: Condens. Matter Mater. Phys.*, 1994, **49**, 1867.
15 N. Islam, *et al.*, *Crystals*, 2022, **12**, 1581.
16 A. M. Nahhas, *et al.*, *Am. J. Nanomater.*, 2019, **7**, 10–21.
17 H. Cheng, N. Biyikli, J. Xie, Ö. Kurdak and H. Morkoç, *J. Appl. Phys.*, 2009, **106**, 103702.
18 S. Samanta, *et al.*, *J. Semicond.*, 2023, **44**, 103101.
19 J. Wang, *et al.*, *Appl. Sci.*, 2022, **12**, 3822.
20 C. S. Knox, *et al.*, *Phys. Rev. B*, 2020, **102**, 045310.
21 B. K. Ridley, *Rep. Prog. Phys.*, 1991, **54**, 169.
22 S. Das Sarma, J. K. Jain and R. Jalabert, *Phys. Rev. B: Condens. Matter Mater. Phys.*, 1990, **41**, 3561–3571.
23 J. S. Bhat, S. B. Kapatkar, S. S. Kubakaddi and B. G. Mulimani, *Phys. Status Solidi B*, 1998, **209**, 37–47.
24 G.-Q. Hai and F. M. Peeters, *Phys. Rev. B: Condens. Matter Mater. Phys.*, 1999, **60**, 8984–8991.
25 C.-J. Zhang and K.-X. Guo, *Phys. E*, 2007, **39**, 103–108.
26 H. T. P. Thuy and N. D. Hien, *J. Phys. Chem. Solids*, 2026, **209**, 113238.
27 G. Weber and J. F. Ryan, *Phys. Rev. B: Condens. Matter Mater. Phys.*, 1992, **45**, 11202–11208.
28 G. Q. Hai, F. M. Peeters and J. T. Devreese, *Phys. Rev. B: Condens. Matter Mater. Phys.*, 1993, **48**, 4666–4674.
29 I. Vurgaftman, J. R. Meyer and L. R. Ram-Mohan, *J. Appl. Phys.*, 2001, **89**, 5815–5875.
30 X. X. Liang and Z. Yan, *Surf. Sci.*, 1998, **400**, 232–238.
31 J.-J. Shi, *Phys. Rev. B: Condens. Matter Mater. Phys.*, 2003, **68**, 165335.
32 I. S. Gradshteyn and I. M. Ryzhik, *Table of Integrals, Series, and Products*, ed. D. Zwillinger and V. H. Moll, Academic Press, Amsterdam, 8th edn, 2015.